# Kv4.2 autism and epilepsy mutation enhances inactivation of closed channels but impairs access to inactivated state after opening

Meng-chin A. Lin[a], Stephen C. Cannon[a,b], and Diane M. Papazian[a,b,c,1]

[a]Department of Physiology, David Geffen School of Medicine at the University of California, Los Angeles, CA 90095-1751; [b]Brain Research Institute, University of California, Los Angeles, CA 90095; and [c]Molecular Biology Institute, University of California, Los Angeles, CA 90095

Edited by Lily Yeh Jan, University of California, San Francisco, CA, and approved March 1, 2018 (received for review September 28, 2017)

**A de novo mutation in the *KCND2* gene, which encodes the Kv4.2 $K^+$ channel, was identified in twin boys with intractable, infant-onset epilepsy and autism. Kv4.2 channels undergo closed-state inactivation (CSI), a mechanism by which channels inactivate without opening during subthreshold depolarizations. CSI dynamically modulates neuronal excitability and action potential back propagation in response to excitatory synaptic input, controlling $Ca^{2+}$ influx into dendrites and regulating spike timing-dependent plasticity. Here, we show that the V404M mutation specifically affects the mechanism of CSI, enhancing the inactivation of channels that have not opened while dramatically impairing the inactivation of channels that have opened. The mutation gives rise to these opposing effects by increasing the stability of the inactivated state and in parallel, profoundly slowing the closure of open channels, which according to our data, is required for CSI. The larger volume of methionine compared with valine is a major factor underlying altered inactivation gating. Our results suggest that V404M increases the strength of the physical interaction between the pore gate and the voltage sensor regardless of whether the gate is open or closed. Furthermore, in contrast to previous proposals, our data strongly suggest that physical coupling between the voltage sensor and the pore gate is maintained in the inactivated state. The state-dependent effects of V404M on CSI are expected to disturb the regulation of neuronal excitability and the induction of spike timing-dependent plasticity. Our results strongly support a role for altered CSI gating in the etiology of epilepsy and autism in the affected twins.**

A-type current | closed-state inactivation | $K^+$ channel gating | gain-of-function mutation | somatodendritic

Recently, a de novo mutation in the *KCND2* gene was identified by exome sequencing in monozygotic twin boys with intractable seizures starting in infancy, autism, and intellectual disability (1). *KCND2* encodes the Kv4.2 voltage-gated $K^+$ channel. Kv4.2 and other members of the Kv4 family serve as the pore-forming subunits in inactivating, somatodendritic A-type $K^+$ ($I_{SA}$) channels, which are widely expressed in the brain (2–8). Kv4.2 is the sole pore-forming subunit in $I_{SA}$ channels found in pyramidal cells in the CA1 region of the hippocampus (6, 7). The hallmark property of $I_{SA}$ channels is the ability to inactivate without opening during subthreshold excitatory postsynaptic potentials (5, 8, 9). This occurs through the mechanism of closed-state inactivation (CSI) (5, 10). CSI determines the steady-state availability of $I_{SA}$ channels and thereby controls resting excitability and firing frequency (5, 8, 9). In addition, CSI temporarily increases excitability in response to excitatory synaptic input, boosting the back propagation of action potentials and $Ca^{2+}$ influx into dendrites (7, 11–17). As a result, CSI is a key component in mechanisms of spike timing-dependent synaptic plasticity (13, 17). We previously reported that V404M, the Kv4.2 mutation associated with epilepsy and autism, impairs CSI, but the underlying mechanism has not been characterized (1).

Voltage-gated $K^+$ channels, such as Kv4.2, contain a tetrameric assembly of pore-forming subunits (18). Each subunit contains six transmembrane segments, S1–S6, and a reentrant loop (Fig. 1*A*). Segments S1–S4 from each subunit form the four peripherally located voltage sensor domains, whereas the single central pore for ion permeation is formed by S5, S6, and the reentrant loop, which functions as the $K^+$ selectivity filter (18). In response to depolarization, the voltage sensor domains undergo several conformational changes between closed states before opening of the pore (Fig. 1*B*) (10, 21). Voltage sensor transitions lead to an activated conformation, C*, that is permissive for pore opening, a cooperative step in which the so-called bundle-crossing gate formed by the S6 segments opens to permit ion flow through the channel (27–29). Coupling between the voltage sensor domain and the pore gate is mediated by residues in the S4–S5 linker, which interact with residues in S6 that form the gate (Fig. 1*A*) (22, 30, 31). The V404M mutation is located in S6 immediately after the conserved sequence proline–valine–proline (PVP), which bends to open the pore gate (Fig. 1*A*) (29). Residue V404 in Kv4.2 is known to be centrally involved in operation of the pore gate, in coupling voltage sensor conformational changes to the gate, and in CSI (10, 22, 26, 32).

The mechanism of CSI is distinct from common forms of inactivation that are tightly coupled to pore opening, such as N-type inactivation, in which a tethered blocker domain occludes the open mouth of the pore, and C-type inactivation, which is thought to involve conformational changes at the selectivity

## Significance

Neuronal somatodendritic A-type potassium channels inactivate without opening in response to subthreshold depolarizations. Closed-state inactivation dynamically modulates excitability and regulates changes in synaptic strength. A mutation, V404M, in the Kv4.2 channel subunit is associated with infant-onset epilepsy and autism. Surprisingly, V404M enhances inactivation of channels that have not opened but dramatically impairs inactivation after opening. We show that increased side-chain volume is largely responsible for these seemingly paradoxical effects. Our results support the conclusion that open channels must close before inactivating and in contrast to previous proposals, suggest that voltage sensor and pore domains of the channel do not dissociate during inactivation. We propose that disruption of closed-state inactivation underlies epilepsy and autism in affected individuals.

Author contributions: M.-c.A.L. and D.M.P. designed research; M.-c.A.L., S.C.C., and D.M.P. performed research; M.-c.A.L. and D.M.P. analyzed data; and D.M.P. wrote the paper.

The authors declare no conflict of interest.

This article is a PNAS Direct Submission.



[1]To whom correspondence should be addressed. Email: papazian@mednet.ucla.edu.

This article contains supporting information online at www.pnas.org/lookup/suppl/doi:10.1073/pnas.1717082115/-/DCSupplemental.

Published online March 26, 2018.

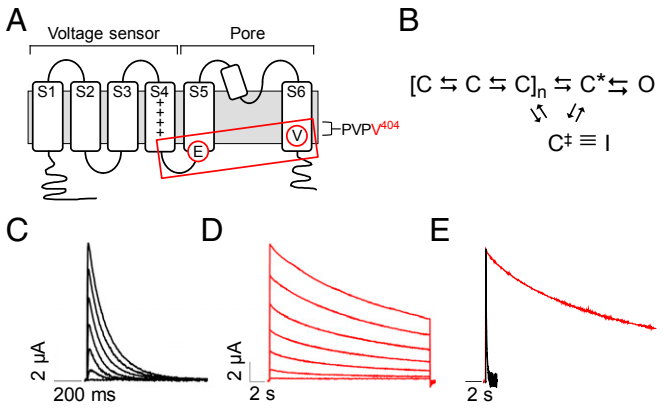


**Fig. 1.** V404M significantly slows macroscopic current decay. (*A*) Membrane topology of Kv4.2 subunit is shown. The voltage sensor (transmembrane segments S1–S4) and pore (S5, S6, and reentrant loop) domains are bracketed. Control of channel activity by voltage is primarily due to positively charged residues (+) in the S4 segment (19, 20). Circled residues indicate the approximate locations of V404 in S6 immediately after the PVP motif and E323 in the S4–S5 linker. Voltage sensor is coupled to the pore gate by interactions between S4–S5 linker and S6 gate residues, including V404 (boxed). (*B*) Highly simplified gating scheme shows essential features of CSI based on available evidence (10, 21–25). In response to depolarization, the voltage sensor domain undergoes transitions between closed states to reach an activated conformation, C*, that is permissive for pore opening. The channel inactivates preferentially from partially activated closed conformations or C*. For CSI, the voltage sensor transitions to an alternative conformation, $C^{‡}$, that corresponds to the inactivated state (I) if the pore gate is closed. Reflecting evidence that open channels must close to inactivate, there is no direct pathway between the open and inactivated states (25, 26). (*C* and *D*) Representative current traces from (*C*) wild-type Kv4.2 (black traces) or (*D*) V404M (red traces). In this figure and subsequent figures, wild-type and mutant Kv4.2 constructs were coexpressed with KChIP3a. Note that V404M currents are shown on a compressed time base. Currents were evoked by pulsing from −100 mV to voltages from −60 to +60 mV. Traces shown were obtained at 20-mV increments. (*E*) Representative wild-type (black) and V404M (red) currents recorded at +20 mV were scaled to the same amplitude and overlaid. Traces are shown on the same time base.

filter located near the extracellular mouth of the pore (23, 33–35). In contrast, CSI in Kv4 channels is coupled to voltage sensor conformational changes evoked by depolarization rather than to pore opening (5, 10, 24). From partially or fully activated closed states, the voltage sensor can enter an alternative conformation, $C^{‡}$, in which the bundle-crossing gate becomes reluctant to open (Fig. 1*B*) (5, 21, 22). Evidence suggests that the bundle-crossing gate is responsible for occluding the pore in the inactivated conformation. Accordingly, open channels would need to close to inactivate (22, 24, 25).

Previously, we showed that the V404M mutation dramatically slows macroscopic current decay and decreases steady-state inactivation during prolonged depolarizations (1). These effects are dominant when V404M and wild-type Kv4.2 subunits are coexpressed at a 1:1 ratio and are evident in the presence of auxiliary $K^+$ channel interacting protein (KChIP) and dipeptidyl peptidase-like protein (DPP) subunits (1), which associate with Kv4 subunits in vivo to form $I_{SA}$ channels (8, 36–38). We have now investigated the mechanism by which V404M alters CSI. Our data indicate that the V404M mutation has a unique combination of seemingly paradoxical, state-dependent effects on inactivation gating in Kv4.2 channels. Surprisingly, we found that the CSI mechanism is intact in mutant channels. Indeed, despite the effect of V404M on the kinetics of macroscopic current decay, the mutation increases the stability of the inactivated state. As a result, inactivation directly from preopen closed states is enhanced in mutant channels compared with wild-type Kv4.2. However, inactivation is severely impaired after the channel opens, because V404M dramatically slows the rate of pore closure, consistent with evidence that open Kv4.2 channels must close to inactivate (24–26). We also find that the increase in side-chain volume that occurs in the valine-to-methionine mutation plays a key role in the kinetic changes in gating seen in V404M channels. A size-compensating, conservative mutation of a nearby interacting residue reverts channel properties to resemble those of wild-type Kv4.2. Due to the state-dependent effects of V404M on CSI, our results indicate that the V404M mutation will have complex, voltage-dependent effects on excitability and synaptic plasticity in the hippocampus and elsewhere in the brain (5, 7, 8, 11–17). Our results strongly support a causative role for the V404M mutation in Kv4.2 in the clinical phenotype of infant-onset epilepsy, autism, and intellectual disability in twin boys who carry the mutation (1).

## Results

**CSI Mechanism Is Intact in V404M Channels.** Wild-type Kv4.2 or the V404M mutant was expressed in *Xenopus* oocytes with KChIP3a, an auxiliary subunit that removes the vestigial N-type, open-state inactivation of Kv4.2 channels, making it feasible to study CSI gating in isolation (39–42). The functional properties of wild-type and mutant channels were analyzed using a two-electrode voltage clamp (43, 44). Expression of V404M generated robust currents that decayed extremely slowly compared with wild-type Kv4.2 (Fig. 1 *C–E*), indicating that the mutation dramatically impairs access to the inactivated state after the channel opens (1). Similar results were obtained when wild-type Kv4.2 or the V404M mutant was coexpressed with KChIP3a and DPP6s (Fig. S1*A*).

Despite the slow decay of macroscopic V404M currents, a prepulse inactivation experiment revealed that the CSI mechanism is intact in mutant channels (Fig. 2 *A–C* and Fig. S1*B*). From −110 mV, the membrane was stepped to prepulse potentials from −130 to +10 mV before a test pulse to measure the remaining current amplitude. The extent of inactivation during the prepulse was determined from the ratio of the remaining current amplitude to the maximal current amplitude measured in the absence of the prepulse. Wild-type Kv4.2 channels that opened during the prepulse (Fig. 2*A*, e.g., magenta trace) or the test pulse rapidly inactivated (Fig. 2*A*). Wild-type channels were maximally inactivated at the steady state at −40 mV and more positive voltages (Fig. 2*C*). In V404M channels, significant CSI occurred at voltages where the probability of channel opening is low, similar to the wild type (Fig. 2*B*, e.g., green trace). In contrast, V404M channels that opened during either the prepulse or the test pulse exhibited little subsequent inactivation (Fig. 2*B*, e.g., cyan trace). Plotting the normalized current amplitude during the test pulse vs. prepulse potential showed that V404M channels undergo CSI, with maximal inactivation occurring at a prepulse voltage of approximately −60 mV, which inactivated more than 80% of the channels (Fig. 2*C*). In contrast to the wild type, however, CSI was significantly less effective at more positive prepulse voltages that open the channel, consistent with the extremely slow decay of macroscopic V404M currents (Fig. 2*C*).

V404M shifted the inactivation curve by approximately −10 mV compared with the wild type (Fig. 2*C*), whereas it shifted the peak conductance voltage curve by about +6 mV with no change in slope (Fig. 2*D*). In Kv4 channels, shifts in the activation and inactivation curves are not coupled, because channels need not open before inactivating (10).

**Closed V404M Channels Inactivate More Rapidly than the Wild Type, but V404M Dramatically Slows Inactivation After Opening.** We compared the kinetics of CSI from preopen closed states and from the open state in the wild type and V404M channels (Fig. 3*A*). To characterize the kinetics of inactivation directly from closed states,

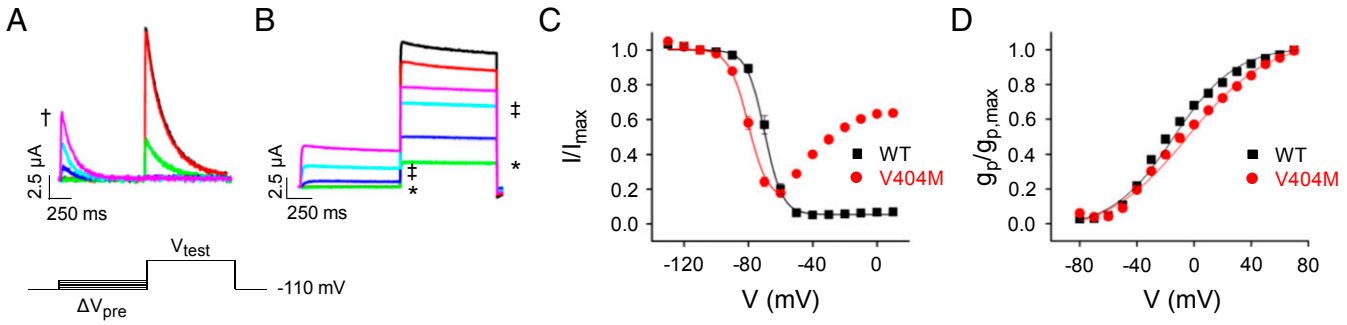


**Fig. 2.** CSI mechanism is intact in V404M channels. (*A* and *B*) Representative current traces evoked by prepulse inactivation protocol from (*A*) wild-type Kv4.2 or (*B*) V404M are shown. From −110 mV, the membrane was stepped for 1 s to prepulse voltages from −130 to +10 mV in 10-mV increments before a test pulse to +60 mV. The traces shown correspond to prepulse voltages of −110 mV (black), −90 mV (red), −70 mV (green; labeled with * in *B*), −50 mV (blue), −30 mV (cyan; labeled with ‡ in *B*), and −10 mV (magenta; labeled with † in *A*). (*C*) Peak current amplitudes at +60 mV were normalized to the peak current amplitude obtained in the absence of a prepulse and plotted vs. prepulse voltage. Wild-type (■) and V404M (red ●) data were fitted with single Boltzmann functions (solid curves). For V404M, only data obtained using prepulses from −130 to −70 or −60 mV were fitted due to reduced inactivation at more positive potentials. Fitted values of the midpoint voltage ($V_{1/2,inact}$) and the slope factor (*k*), provided as mean ± SEM, were the wild type ($n = 18$), −69 ± 1 and 4 ± 0.2 mV, respectively, and V404M ($n = 21$), −80 ± 1 and 5 ± 0.2 mV, respectively. Values of $V_{1/2,inact}$ differed significantly ($P < 0.00001$ by ANOVA followed by Student's *t* test). (*D*) Currents were evoked by stepping for 150 ms from −100 mV to voltages from −60 to +90 mV in 10-mV increments. Peak conductance at each voltage was calculated from peak current amplitude, normalized to the maximum peak conductance, and plotted vs. voltage. Wild-type (■) and V404M (red ●) data were fitted with single Boltzmann functions (solid curves). Fitted values of the midpoint voltage ($V_{1/2,act}$) and the slope factor (*k*), provided as mean ± SEM, were the wild type ($n = 10$), −17 ± 2 and 21 ± 0.5 mV, respectively, and V404M ($n = 12$), −9 ± 2 and 22 ± 1 mV, respectively. Values of $V_{1/2,act}$ differed significantly ($P < 0.005$). It should be noted that the shallowness of the peak conductance–voltage curves makes it difficult to obtain reliable estimates of $V_{1/2,act}$. WT, wild type.

a prepulse inactivation protocol was applied using prepulses of varying durations. The current amplitude during the test pulse was plotted vs. prepulse duration, and the data were fitted with a single exponential function to estimate the inactivation time constant, $\tau_{inact}$. To characterize the kinetics of inactivation after opening, a single exponential function was fitted to the decay of macroscopic currents evoked by step depolarizations. Values of $\tau_{inact}$ obtained from these protocols were plotted vs. prepulse voltage or step voltage (Fig. 3 *B*–*D*).

In wild-type channels, the onset of inactivation directly from the closed state became faster with increasing depolarization until –40 mV (Fig. 3*B*). As the open probability increased at more positive voltages, however, CSI was progressively slower. Similar results have been reported previously, providing evidence that Kv4.2 channels preferentially inactivate from preopen closed states (24–26, 37). According to this proposal, inactivation is slower after opening, because open channels must close before inactivating.

V404M channels inactivated rapidly from preopen closed states (Fig. 3*C*). Surprisingly, given the slow decay of macroscopic V404M currents, inactivation from the closed state was significantly faster in mutant channels, with $\tau_{inact}$ values that were 2.1- to 4.6-fold less in V404M than in wild-type channels over the tested voltage range (Fig. 3*D*). In contrast, the inactivation of V404M channels after opening was extremely slow, as expected from macroscopic current traces (Fig. 3*C*). The difference in inactivation kinetics from open and closed states was striking at voltages between –50 and –20 mV, where both the open- and closed-state protocols were applied (Fig. 3*C*, boxed area). These data account for the results of the prepulse inactivation experiment, in which little current decay was observed in V404M channels that opened during prepulses, despite the fact that significant inactivation occurred at those voltages (Fig. 2*B*, e.g., cyan trace).

It is important to note that time constant values obtained by fitting macroscopic current decay of V404M channels are likely to be underestimated, because the rate of decay depended on current amplitude, with larger amplitudes decaying more rapidly, even with constant perfusion (Fig. S2). These results suggest that part of the decline in mutant current amplitude during long pulses results from the accumulation of extracellular $K^+$, which would decrease the driving force on $K^+$ and thereby, decrease current amplitude.

**V404M Dramatically Slows Deactivation.** Given the evidence that Kv4.2 channels inactivate preferentially from preopen closed states (24–26, 37), we tested the hypothesis that the V404M mutation dramatically slows inactivation after opening by significantly decreasing the rate of pore closure. After opening channels with a depolarizing pulse, the kinetics of closing at voltages between −120 and −45 mV were estimated by fitting a single exponential function to tail current decay to obtain values of the deactivation time constant, $\tau_{deact}$ (Fig. 4). V404M slowed channel closing dramatically over the tested voltage range, with $\tau_{deact}$ values that were 50- to 200-fold greater in mutant than in wild-type channels (Fig. 4*B*). These results suggest that V404M specifically inhibits inactivation after opening by dramatically reducing the rate at which the pore gate closes.

**V404M Does Not Alter the Time Constant of Pore Opening.** To investigate the effect of V404M on pore opening, the kinetics of the opening transition were characterized using a two-pulse reactivation protocol (45). After a brief pulse from −100 to +60 mV to maximally open channels, the membrane was repolarized to −100 mV for a variable time ($\Delta t$) before a second test pulse to +60 mV was applied (Fig. 5 *A* and *B*). If $\Delta t$ is sufficiently short, the channel should return only to the most proximal closed state, C*, in which case the second pulse should isolate the opening (C* to O) transition (Fig. 1*B*). Although this may not be perfectly achieved, when $\Delta t$ is short, the kinetics of opening during the second pulse should approach that of the opening transition. This protocol revealed that the minimum value of the activation time constant during the second pulse ($\tau_{act}$) did not differ significantly between mutant and wild-type channels (Fig. 5 *C* and *D*). Thus, the V404M mutation dramatically slows the kinetics of pore closing (Fig. 4) while having little effect on the kinetics of the opening transition (Fig. 5 *C* and *D*).

Because V404M dramatically slows deactivation compared with the wild type (Fig. 4), it was necessary to use longer interpulse intervals to estimate reactivation kinetics in mutant channels (Fig. 5 *B* and *C*). Similarly, returning to the original activation kinetics took significantly longer in V404M channels than in the wild type,

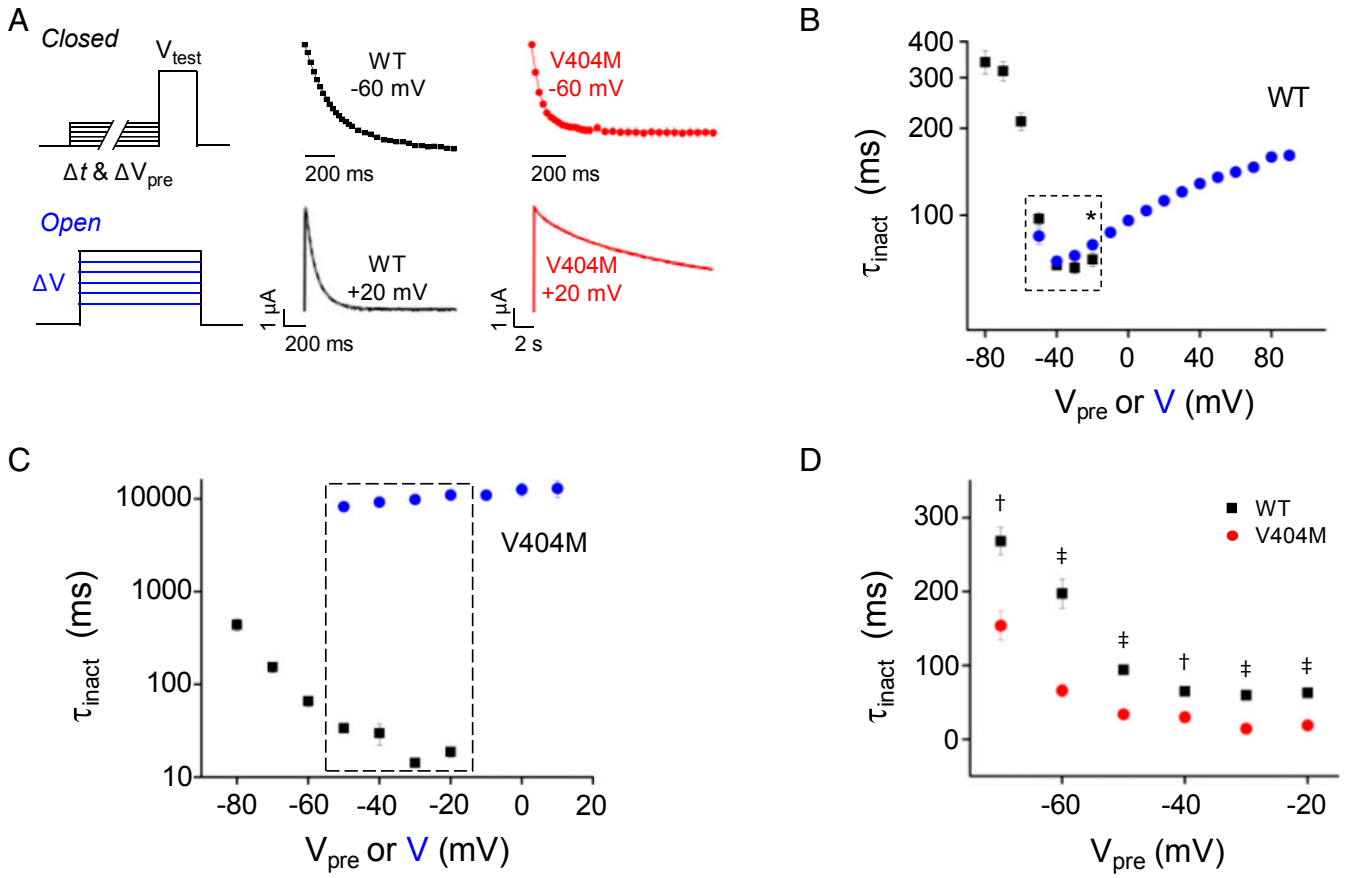


**Fig. 3.** V404M dramatically slows inactivation after opening but accelerates inactivation from closed states. (*A*, *Upper Left*) To characterize the kinetics of inactivation from partially or fully activated closed states, the membrane was stepped from −100 mV to prepulse voltages from −80 to −20 mV for durations from 0 to 1,056 ms before a test pulse to +20 mV. [*A*, *Upper Center* (wild-type Kv4.2) and *Upper Right* (V404M)] Current amplitude at +20 mV was normalized to the current amplitude obtained in the absence of a prepulse (i.e., $\Delta t = 0$) and plotted vs. $\Delta t$. Representative data obtained after a prepulse to −60 mV are shown. The data were fitted with a single exponential function to estimate the inactivation time constant, $\tau_{inact}$. Fits are shown superimposed on the data. (*A*, *Lower Left*) To characterize the kinetics of inactivation after opening, the membrane was depolarized from −100 mV to voltages from −50 to +90 mV for 1.5 s (wild-type Kv4.2) or 21.5 s (V404M). [*A*, *Lower Center* (wild-type Kv4.2) and *Lower Right* (V404M)] Representative current traces recorded at +20 mV are shown. Macroscopic current decay was fitted with a single exponential function to estimate the inactivation time constant, $\tau_{inact}$. Fits are shown superimposed on the data (dashed gray curves). (*B* and *C*) Values of $\tau_{inact}$ for (*B*) wild-type Kv4.2 and (*C*) V404M obtained using the closed-state (■) and open-state (blue ●) protocols have been plotted on a log scale vs. prepulse or step voltage, respectively. Values are provided as mean ± SEM (wild-type, $n = 5$–14; V404M, $n = 4$–10). Both protocols were applied at prepulse or step voltages from −50 to −20 mV (dashed boxes). (*B*) In wild-type channels, values of $\tau_{inact}$ obtained at −20 mV from the closed-state (70 ± 4 ms) and open-state (79 ± 1 ms) protocols differed significantly ($n = 10$). *$P < 0.05$. (*C*) In V404M channels, values of $\tau_{inact}$ obtained by the closed- and open-state protocols differed significantly from −50 to −20 mV ($P < 0.00001$, $n = 5$–10). (*D*) Values of $\tau_{inact}$ obtained using the closed-state protocol for wild-type Kv4.2 (■; $n = 5$–12) and V404M (red ●; $n = 7$–10) have been plotted vs. prepulse voltage. Values of $\tau_{inact}$, provided as mean ± SEM, differed significantly at all voltages. †$P < 0.0001$; ‡$P < 0.00001$. WT, wild type.

reflecting the increased time needed to close mutant channels to reestablish the initial conditions (Fig. 5 *B* and *C*). During the first pulse, apparent activation kinetics were faster in wild-type than in mutant channels (Fig. 5 *C*, symbols at $\Delta t = 0$, and *E*). This likely reflects competition between activation and the inactivation of open channels that occurs in the wild type but is significantly reduced in mutant channels due to the dramatic impairment of inactivation after pore opening.

**V404M Significantly Slows Recovery from Inactivation.** Our data show that V404M accelerates the onset of inactivation from preopen closed states (Fig. 3*D*). To further investigate the effect of the mutation on the stability of the inactivated state, we compared the kinetics of recovery from inactivation in wild-type and mutant channels (Fig. 6). Maximal inactivation was induced from the closed state by applying a prepulse to −40 mV (the wild type) or −60 mV (V404M). The membrane was then stepped for varying durations to recovery voltages between −120 and −80 mV. The extent of recovery was determined by measuring peak current amplitude during a test pulse to +60 mV, which was normalized to the maximal current amplitude in the absence of the inactivating prepulse and plotted vs. recovery time (Fig. 6 *A* and *B*). The data were fitted with a single exponential function to estimate the time constant of recovery, $\tau_{rec}$. The V404M mutation dramatically slowed the kinetics of recovery from inactivation, increasing $\tau_{rec}$ by 3.3- to 5.4-fold compared with wild-type channels over the tested voltage range (Fig. 6*C*). Thus, we find that V404M accelerates the onset of inactivation from preopen closed states and slows recovery from inactivation. These data indicate that the V404M mutation increases the relative stability of the inactivated state. Taken together, our results indicate that the V404M mutation significantly enhances the inactivation of closed channels but dramatically impairs inactivation after opening by slowing closure of the pore gate.

**Increase in Side-Chain Volume Contributes Substantially to Functional Effects of V404M Mutation.** To investigate the mechanism by which V404M alters inactivation gating, we tested the hypothesis that an increase in side-chain volume makes a significant contribution to

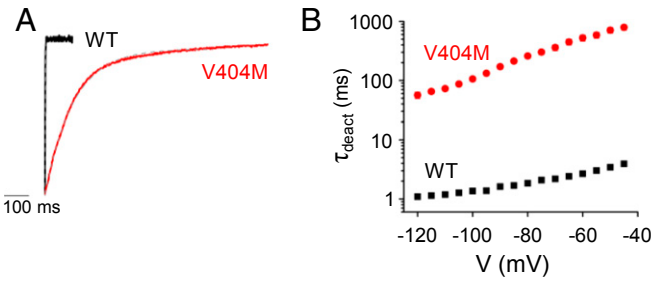


**Fig. 4.** V404M dramatically slows pore closing. (*A*) Representative scaled and overlaid tail currents from wild-type (black) and V404M (red) channels were recorded on repolarization from +60 to −100 mV in a 98 mM KCl bath solution. Tail current decay was fitted with a single exponential function (dashed gray curve) to estimate the deactivation time constant ($\tau_{deact}$). (*B*) Values of $\tau_{deact}$ for the wild type (■; $n = 24$) and V404M (red ●; $n = 29$) have been plotted on a log scale vs. tail potential. Values of $\tau_{deact}$, provided as mean ± SEM, differed significantly at all voltages ($P < 0.00001$). WT, wild type.

the mutant phenotype. Replacing valine 404 with methionine increases the volume of the side chain by ∼20% from 139 to 168 Å$^3$ (46). To compensate for the volume increase, we introduced a second site mutation at a nearby residue. We chose E323, a conserved acidic residue at the cytoplasmic end of the S5 segment (Fig. 1*A*), for the following reasons. Thermodynamic double-mutant cycle analysis indicates that V404 interacts with residues in the S4–S5 linker and the cytoplasmic end of S5 during CSI, with particularly strong energetic coupling to E323 (22). Previously, the same approach had identified the analogous residues in Shaker, V476, and E395 as exhibiting strong energetic coupling during voltage-dependent activation (30). Consistent with these results, high-resolution X-ray structures of Kv1.2 and a Kv1.2/Kv2.1 chimera and a homology model of Kv4.2 based on those structures show that these residues are within atomic proximity (Fig. 7*A*) (18, 22, 47, 48). Fortuitously, the conservative E323D mutation compensates well for V404M, decreasing side-chain volume by ∼18% (141 Å$^3$ in glutamate vs. 117 Å$^3$ in aspartate) without changing the acidic character of the side chain (46). As a result, the total volume of aspartate plus methionine differs by less than 2% from the original glutamate and valine residues.

We generated the single E323D and double E323D+V404M mutants, which were expressed in oocytes in the presence of KChIP3a for functional analysis. The E323D and E323D+V404M constructs generated active channels that activated and inactivated in a more depolarized voltage range than wild-type Kv4.2 (Fig. S3). We assessed whether introducing the E323D mutation rescued those channel properties most significantly affected by V404M, namely the kinetics of inactivation, deactivation, and recovery from inactivation (Fig. 7).

Macroscopic E323D currents inactivated rapidly, similar to the wild type (compare Fig. 7*B* with Fig. 1*C*). Strikingly, combining the E323D mutation with V404M restored rapid decay of the macroscopic current (Fig. 7*C*). It was infeasible to compare decay kinetics for the wild type, V404M, E323D, and E323D+V404M at the same voltage, because the E323D mutation, alone or with V404M, dominantly shifts the voltage dependence of activation (Fig. S3) and because inactivation becomes slower as the probability of opening increases (Fig. 3*B*). We, therefore, compared the minimum values of $\tau_{inact}$ obtained by fitting macroscopic current decay to approximate the fastest kinetics of inactivation after opening (Fig. 7*D*). In contrast to V404M, values of $\tau_{inact,min}$ for the E323D+V404M double mutant and the E323D single mutant were in the same range as the wild type (Fig. 7*D*).

We used the prepulse protocol shown in Fig. 3*A* to characterize the kinetics of inactivation from partially or fully activated closed states. Again, it was infeasible to compare the onset of inactivation in all of the constructs at a single voltage due to the depolarized shift caused by the E323D mutation (Fig. S3). We, therefore, fitted plots of $\tau_{inact}$ vs. prepulse voltage with single exponential functions to estimate the minimum values of $\tau_{inact}$ from the closed state for each construct (Fig. S4). In contrast to V404M, $\tau_{inact,min}$ values in E323D+V404M and E323D channels did not differ significantly from that of the wild type (Fig. 7*E*).

In V404M, slow closing of the pore gate dramatically slows the inactivation of open channels (Fig. 4) (26). In contrast, the kinetics of deactivation in double-mutant E323D+V404M channels did not differ significantly from the wild type over a large voltage range (Fig. 7*F*). Interestingly, deactivation was significantly faster in the E323D single mutant than in the wild type between −90 and −45 mV. Reduction of side-chain volume at position 323 may contribute to this effect, which is opposite to that of V404M.

To compare the kinetics of recovery from inactivation, maximal inactivation was induced by pulsing to +60 mV (the wild type, E323D) or +80 mV (E323D+V404M), followed by repolarization to −100 mV for varying durations. The kinetics of recovery from inactivation did not differ significantly in wild-type, E323D, and E323D+V404M channels (Fig. 7*G*). Thus, the kinetics of inactivation

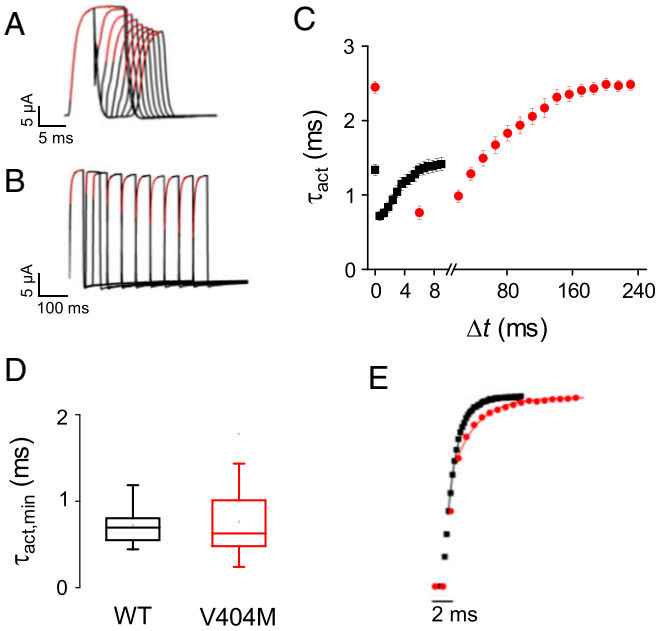


**Fig. 5.** V404M does not alter apparent kinetics of pore opening. The kinetics of the pore-opening transition were estimated by a two-pulse protocol, in which the membrane was stepped twice from −100 to +60 mV separated by an interpulse interval of variable duration (Δ*t*) (45). (*A* and *B*) Representative current traces recorded during the second pulse to +60 mV (black) are shown for (*A*) wild-type Kv4.2 and (*B*) V404M. Currents recorded after interpulse intervals of various durations have been superimposed. Note that V404M currents are shown on a compressed time base. Traces were fitted with a single exponential function (red) to estimate the time constant of activation ($\tau_{act}$). (*C*) Values of $\tau_{act}$ for the wild type (■) and V404M (red ●) during the second pulse have been plotted vs. interpulse interval (Δ*t*). Note the break in the timescale. Symbols at $\Delta t = 0$ ms indicate values of $\tau_{act}$ obtained during the first pulse (*E*). (*D*) Box plot shows the minimum values of $\tau_{act}$ ($\tau_{act,min}$) from *C* obtained after the shortest interpulse interval for the wild type (black) and V404M (red). Mean values of $\tau_{act,min}$ ± SEM were the wild type ($n = 11$), 0.72 ± 0.06 ms and V404M ($n = 20$), 0.76 ± 0.09 ms. These values did not differ significantly. (*E*) The kinetics of opening in the wild type (■) and V404M (red ●) during the first pulse to +60 mV are compared. The discontinuous current traces reflect the experimental sampling rates. Data have been scaled to the same amplitude and overlaid. Single exponential fits to the data (solid curves) are superimposed (the wild type, black; V404M, red). WT, wild type.

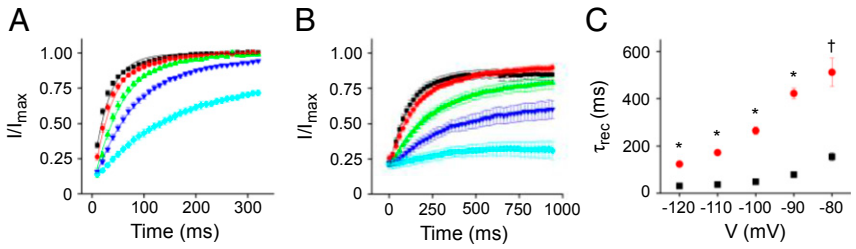


**Fig. 6.** V404M significantly slows recovery from inactivation. (*A*) Wild-type and (*B*) V404M channels were maximally inactivated from the closed state by pulsing to −40 mV (the wild type) for 500 ms or −60 mV (V404M) for 1 s before repolarizing for various durations to recovery voltages from −120 to −80 mV (−80 mV, cyan; −90 mV, blue; −100 mV, green; −110 mV, red; −120 mV, black). Remaining peak current amplitude was measured in a subsequent test pulse to +60 mV, normalized to the maximum peak current amplitude at +60 mV, and plotted vs. recovery time. Data, shown as mean ± SEM, were fitted with a single exponential function to estimate $\tau_{rec}$. Fits (solid curves) are shown superimposed on the data. (*C*) Values of $\tau_{rec}$ for the wild type (■; $n = 5$) and V404M (red ●; $n = 8$) have been plotted vs. recovery voltage. Values of $\tau_{rec}$ differed significantly at every voltage. *$P < 0.00001$; †$P < 0.0005$.

onset from the closed state and of recovery from inactivation were similar in wild-type and E323D+V404M channels. These results indicate that combining the E323D mutation with V404M decreases the stability of the inactivated state to that of wild-type channels.

Overall, our data indicate that the size-compensating E323D mutation reverses the major effects of V404M on Kv4.2 channel function, including changes in the stability of the inactivated state and the kinetics of macroscopic current decay, inactivation from the closed state, deactivation, and recovery from inactivation. We conclude that the increase in side-chain volume at position 404 makes a major contribution to altered inactivation and deactivation gating in V404M channels.

## Discussion

**V404M Has Opposing, State-Dependent Effects on CSI Gating.** Here, we investigated the mechanism by which V404M, a mutation in Kv4.2 that is associated with epilepsy, autism, and intellectual disability in twin boys, alters CSI gating (1). We found that V404M enhances inactivation from preopen closed states but dramatically impairs access to the inactivated state after the channel opens. In V404M channels, the onset of inactivation before opening is accelerated compared with wild-type channels, whereas recovery from inactivation is slowed. These results indicate that V404M increases the relative stability of the inactivated state. In parallel, the mutation dramatically slows closing of the pore gate, which significantly impairs the inactivation of mutant channels that have opened. The finding that slow pore closing is correlated with dramatically impaired inactivation strongly supports the conclusion that open Kv4.2 channels must close to inactivate by the CSI mechanism (26). Indeed, closing is required if the pore gate is responsible for occluding ion flow in the inactivated state, a proposal that is highly consistent with our data (22, 24–26).

**Role of Side-Chain Volume Suggests That V404M Increases Physical Contact Between Pore Gate and Voltage Sensor.** Our results indicate that increased side-chain volume makes a substantial contribution to the effects of V404M on Kv4.2 gating. We found that E323D, a conservative mutation that compensates for the increase in side-chain volume, rescues the major functional effects of V404M, including changes in the kinetics of inactivation onset and recovery as well as deactivation. Combination with E323D nullifies the opposing effects of V404M, reversing the increased stability of the inactivated state and restoring prominent inactivation after opening. We chose E323, because previous work established that it is physically proximate and functionally coupled to V404 during activation and inactivation gating (22, 30). Importantly, E323 is located in the region that couples the voltage sensor domain to the pore gate (Fig. 1*A*). Our data suggest that the larger methionine residue in V404M increases the binding interface between the gate and the voltage sensor coupling region, thereby strengthening their physical interaction, and that introduction of the E323D mutation reduces the area of interaction to approximate that present in wild-type channels.

Our finding that V404M enhances the stability of the inactivated state is difficult to reconcile with previous proposals that the S4–S5 linker and the S6 pore gate become uncoupled and dissociate from each other on inactivation in Kv4 channels (10, 22, 25, 32). This hypothesis predicts that increased physical contact mediated by methionine would slow uncoupling and thereby, decrease the rate of inactivation. In contrast, V404M accelerates the onset of inactivation from preopen closed states. Furthermore, if the pore gate dissociates on inactivation, it is difficult to account for the finding that a second site mutation in the coupling region restores the rate of recovery from inactivation to that found in wild-type channels. Instead, our data support the conclusion that physical coupling between the pore gate and the voltage sensor domain is maintained in the inactivated state.

**Increasing the Forward Biases of Opening and of Inactivation from Preopen Closed States Can Account for the Functional Properties of V404M Channels.** To identify changes in gating transitions that could underlie the functional effects of V404M, we performed kinetic modeling based on a previously published gating scheme for Kv4.3 expressed with KChIP1 (40). This scheme was modified by eliminating two inactivated states accessed from the open state (40). In the resulting model, sequential voltage-dependent transitions between five closed states, $C_0$ to $C_4$, lead to a single open state, O (Fig. 8*A*). Voltage-independent transitions lead from the closed states to five parallel inactivated states, $I_0$ to $I_4$. An allosteric factor $f$ increases the probability of inactivation as the channel transits toward $C_4$. Inactivation from the open state requires channel closure.

Using initial rate constant values from the previously published model (40), wild-type data were fitted to this scheme (Table 1). Simulations indicated that the model reasonably reproduced wild-type currents elicited by a variety of pulse protocols as well as the prepulse inactivation curve (Fig. 8 *B* and *C*). To fit V404M data, $\alpha_{(V)}$ and $\beta_{(V)}$ were fixed to the fitted wild-type values, and all other rate constants were allowed to vary. Increasing the forward biases of opening and of inactivation from preopen closed states was sufficient to simulate the major functional properties of V404M, including the kinetics of macroscopic current decay, deactivation, and inactivation onset and recovery (Fig. 8*D* and Table 1). The unusual prepulse inactivation curve of V404M channels was also replicated (Fig. 8*E*). These results indicate that altering the kinetics of voltage-dependent transitions between closed states is not required to simulate the properties of V404M.

Due to competition between CSI and opening, Kv4 channels exhibit relatively weak coupling between voltage sensor conformational

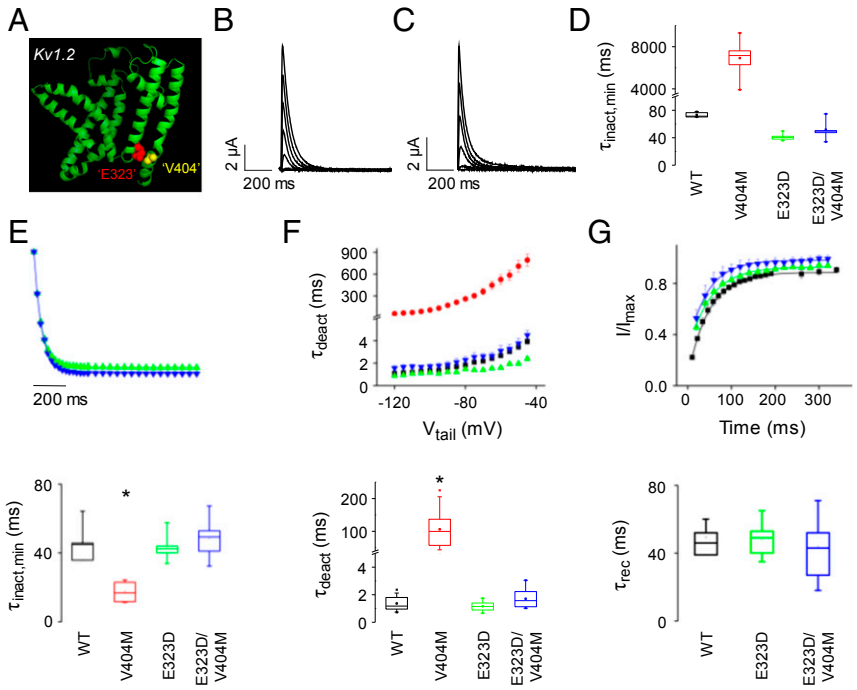


**Fig. 7.** Volume-compensating second site mutation, E323D, reverses effects of V404M on the kinetics of CSI, deactivation, and recovery from inactivation. (*A*) Ribbon diagram shows the peptide backbone of the membrane domain (S1–S6) of Kv1.2 subunit (Protein Data Bank ID code 2A79) (18) with space-filling representations of residues homologous to E323 (red) and V404M (yellow). These residues correspond to E395 and V476 in Shaker. The figure was made using Pymol. (*B*) E323D currents were evoked by stepping from −100 mV to voltages from −60 to +60 mV in 10-mV increments. Representative traces, obtained at 20-mV increments, are shown. (*C*) E323D+V404M currents were evoked by stepping from −100 mV to voltages from −40 to +80 mV in 10-mV increments. Representative traces, obtained at 20-mV increments, are shown. (*D*) Box plot shows minimum values of $\tau_{inact}$ obtained by fitting the decay of macroscopic currents with a single exponential function. Mean values of $\tau_{inact,min}$ ± SEM were the wild type ($n$ = 6), 69 ± 2 ms at −40 mV; V404M ($n$ = 6), 6,912 ± 722 ms at −60 mV; E323D ($n$ = 7), 41 ± 2 ms at 0 mV; and E323D+V404M ($n$ = 8), 52 ± 4 ms at +20 mV. Because it was infeasible to compare values of $\tau_{inact,min}$ for all of the constructs at the same voltage, statistical analysis is not reported. (*E*, *Upper*) Kinetics of inactivation from the closed state at +10 mV for E323D (green ▲; $n$ = 6) and at +20 mV for E323D+V404M (blue ▼; $n$ = 8) were characterized using the closed-state protocol shown in Fig. 3*A*, *Upper Left*. Data are provided as mean ± SEM. (*E*, *Lower*) Box plot shows minimum values of $\tau_{inact}$ ($\tau_{inact,min}$) for the wild type, V404M, E323D, and E323D+V404M. Values of $\tau_{inact,min}$ were obtained by fitting single exponential functions to plots of $\tau_{inact}$ vs. voltage (Fig. S4). Mean values of $\tau_{inact,min}$ ± SEM were the wild type ($n$ = 8), 46 ± 3 ms; V404M ($n$ = 7), 18 ± 2 ms; E323D ($n$ = 5), 44 ± 4 ms; and E323D+V404M ($n$ = 8), 49 ± 4 ms. Value of $\tau_{inact,min}$ for V404M differed significantly from the wild type, E323D, and E323D+V404. *$P$ < 0.00001. (*F*, *Upper*) Values of $\tau_{deact}$, obtained as described in Fig. 4, have been plotted vs. tail voltage for the wild type (■), V404M (red ●), E323D (green ▲), and E323D+V404M (blue ▼). Values of $\tau_{deact}$ in E323D differed significantly from wild-type Kv4.2 ($P$ < 0.01 to $P$ < 0.0001) and E323D+V404M ($P$ < 0.001 to $P$ < 0.0001) between −90 and −45 mV. (*F*, *Lower*) Box plot shows values of $\tau_{deact}$ at −100 mV. Mean values of $\tau_{deact}$ ± SEM were the wild type ($n$ = 24), 1.4 ± 0.1 ms; V404M ($n$ = 29), 105.9 ± 9.3 ms; E323D ($n$ = 15), 1.2 ± 0.1 ms; and E323D+V404M ($n$ = 10), 1.6 ± 0.3 ms. Value of $\tau_{deact}$ for V404M differed significantly from the wild type, E323D, and E323D+V404. *$P$ < 0.00001. (*G*, *Upper*) The wild type (■), E323D (green ▲), and E323D+V404M (blue ▼) were maximally inactivated by pulsing from −100 to +60 mV (the wild type and E323D) or +80 mV (E323D+V404M) for 500 ms. Recovery from inactivation was monitored by repolarizing to −100 mV for various durations before a test pulse to +60 mV (the wild type and E323D) or +80 mV (E323D+V404M). Remaining peak current amplitude during the test pulse was measured, normalized to the peak current amplitude during the first pulse, and plotted vs. recovery time. (*G*, *Lower*) Box plot shows $\tau_{rec}$ at −100 mV for the wild type, E323D, and E323D+V404M. Mean values of $\tau_{rec}$ ± SEM were the wild type ($n$ = 4), 49 ± 4 ms; E323D ($n$ = 13), 48 ± 2 ms; and E323D+V404M ($n$ = 7), 47 ± 6 ms. These values did not differ significantly. WT, wild type.

changes and opening of the pore gate (26, 40). The opening of wild-type channels is not kinetically favored (26, 40). This is recapitulated in the wild-type model, where the ratio of opening and closing rate constants at 0 mV ($k_{co,V=0}/k_{oc,V=0}$) is 0.65 (Table 1). Open channels close and inactivate. As a result, CSI is prominent over a wide voltage range (10, 40). In contrast, modeling indicates that the forward bias of opening in V404M channels is significantly enhanced compared with the wild type by a 3.7-fold increase in the opening rate constant, $k_{co,V=0}$, paired with a dramatic 175-fold decrease in the closing rate constant, $k_{oc,V=0}$ (Table 1). The large decrease in the closing rate constant is consistent with the slow deactivation of V404M channels observed experimentally. The much smaller change in the opening rate is reasonably compatible with the reactivation experiment. Using the fitted values of $k_{oc(V)}$ and $k_{co(V)}$, the time constants of opening, $\tau_{act}$, at +60 mV were estimated to be 2 and 1 ms in wild-type and mutant channels, respectively. These values are in the same range as our experimental results (compare with Fig. 5*D*). Because V404M increases the forward bias of opening substantially, CSI is prominent only at voltages where mutant channels have a low probability of opening.

Modeling indicated that enhancing inactivation from preopen closed states was also required to adequately mimic the functional properties of V404M channels. In the V404M model, the inactivation rate constant was increased eightfold, whereas the recovery rate constant was decreased fourfold compared with the wild type, consistent with our experimental data.

We estimated the occupancy of the open state in wild-type and mutant channels using the simulation program. At +60 mV, estimates of peak occupancy were similar in wild-type (62%) and V404M (67%) channels. In contrast, steady-state occupancy of the open state differed significantly. At the end of a 10-s depolarization to +60 mV, the occupancy of $I_4$ was 96% in wild-type channels but only 63% in V404M, with the remainder of the mutant channels still in the open state.

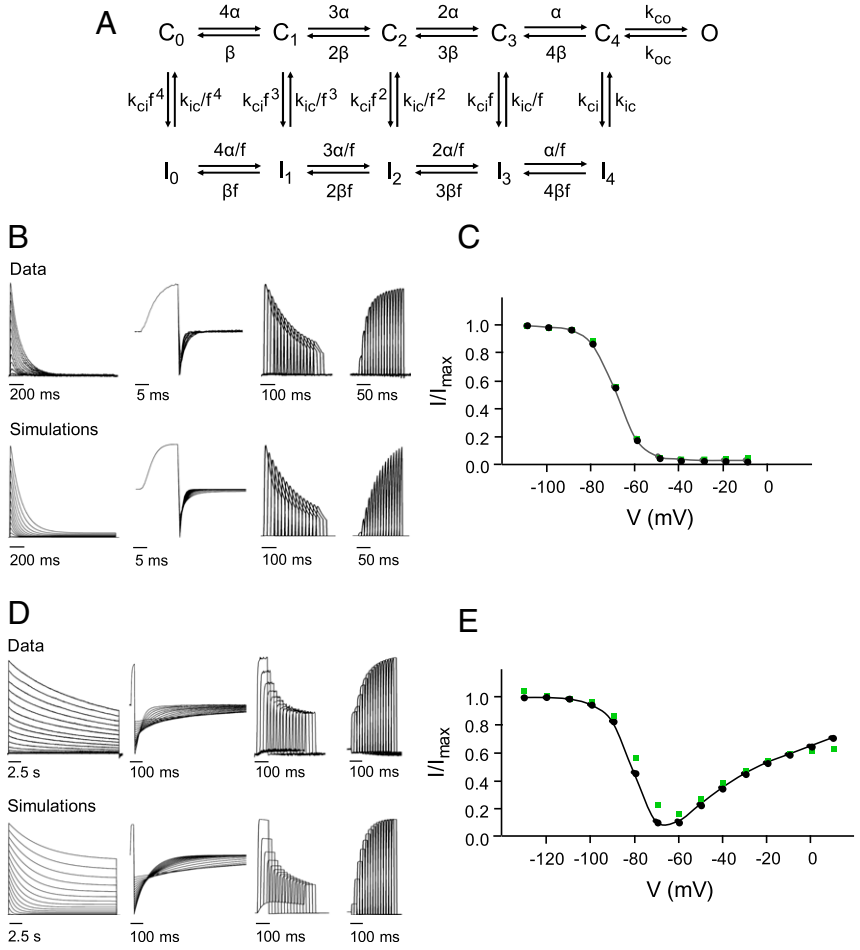


**Fig. 8.** Functional effects of V404M can be simulated by altering the kinetics of open/closed and closed/inactivated transitions. (*A*) Wild-type and V404M data were modeled using a gating scheme with five closed states ($C_0$ to $C_4$), five parallel inactivated states ($I_0$ to $I_4$), and a single open state (O). The scheme is a modified version of a previously published model for Kv4.3 expressed with KChIP1 (40). (*B*) Representative data obtained from wild-type channels (*Upper*) is compared with simulations that were generated using modeled rate constants (*Lower*). From left to right, the panels show evoked currents or simulations corresponding to IV series, deactivation, onset of inactivation at −60 mV, and recovery from inactivation at −120 mV, respectively. Fitted rate constants are provided in Table 1. (*C*) Prepulse inactivation curve for the wild type was constructed from simulated data (black circles and line). For comparison, green squares show experimental data for the wild type from Fig. 2*C*. (*D*) Representative data obtained from V404M channels (*Upper*) are compared with simulations that were generated using modeled rate constants (*Lower*). From left to right, the panels show evoked currents or simulations corresponding to IV series, deactivation, onset of inactivation at −60 mV, and recovery from inactivation at −120 mV, respectively. Fitted rate constants are provided in Table 1. Compared with the wild type, V404M increased the forward bias of opening and inactivation from preopen closed states. (*E*) Prepulse inactivation curve for V404M was constructed from simulated data (black circles and line). For comparison, green squares show experimental data for V404M from Fig. 2*C*.

**V404M Mutation May Enhance Voltage Sensor Relaxation.** During CSI, partially or fully activated voltage sensor domains undergo an alternative transition off the main activation pathway that makes the pore gate reluctant to open (Fig. 1*B*) (10, 21). The available evidence suggests that the inactivated state has two essential features: the voltage sensor in this alternative conformation, $C^{\ddagger}$, and a closed pore gate (21, 25). Recently, Covarrubias and coworkers (10, 21) presented evidence that the voltage sensor conformational change during CSI gating corresponds to relaxation, an inherent transition of activated voltage sensors to a more stable conformation (49). Relaxation is promoted by depolarization and results in an altered energy landscape that affects the steady-state and kinetic properties of voltage sensor return to the resting conformation (49). Relaxation occurs in voltage sensor domains whether or not a pore domain is present (49, 50). In $K^+$ channels, voltage sensor relaxation can occur before or after opening of the pore gate (21, 50–53). Previously, voltage sensor relaxation was thought to underlie open-state C-type inactivation, in which conformational changes at the selectivity filter occlude ion flow (35, 50, 54). However, studies using Kv1.2 and Shaker channels show that the kinetics of voltage sensor relaxation and open-state C-type inactivation are distinct (50). In contrast, in Kv4.2, the steady-state and kinetic properties of CSI and voltage sensor relaxation, detected as apparent immobilization of gating charge, are well-correlated (21).

Our results suggest that the V404M mutation increases the relative stability of the relaxed voltage sensor conformation. In this case, V404M would enhance CSI in channels that have not opened by increasing the rate of relaxation from preopen closed states and decreasing the rate of recovery from the relaxed state. In parallel, V404M dramatically slows gate closing and thereby, impairs CSI after the channel opens. We propose that the V404M mutation may also promote voltage sensor relaxation while the pore is open. Relaxation after opening occurs prominently in channels that, like Shaker, have strong coupling between the voltage sensor domain and the pore gate and a kinetically favored opening transition (50). Importantly, voltage sensor relaxation in the presence of an open gate significantly slows gate closing (50). One interesting possibility

**Table 1. Fitted rate constants**

| Parameter, $s^{-1}$ | Wild type | V404M |
|---|---|---|
| $\alpha_{V=0}$ | 450 | 450 |
| $\alpha_1$ | 0.23 | 0.23 |
| $\beta_{V=0}$ | 2 | 2 |
| $\beta_1$ | 2.2 | 2.2 |
| $k_{co,V=0}$ | 160 | 590 |
| $k_{co,1}$ | 0.27 | 0.13 |
| $k_{oc,V=0}$ | 245 | 1.4 |
| $k_{oc,1}$ | 0.33 | 0.40 |
| $k_{ci}$ | 25 | 200 |
| $k_{ic}$ | 0.3 | 0.07 |

Voltage-dependent rate constants are defined as $\alpha_{(V)} = \alpha_{V=0} \times \exp(\alpha_1 \times VF/RT)$, $\beta_{(V)} = \beta_{V=0} \times \exp(-\beta_1 \times VF/RT)$, $k_{co,(V)} = k_{co,V=0} \times \exp(k_{co,1} \times VF/RT)$, and $k_{oc,(V)} = k_{oc,V=0} \times \exp(-k_{oc,1} \times VF/RT)$. Fitted values of the allosteric factor $f$: the wild type, 0.37; V404M, 0.25.

is that V404M increases the rate of voltage sensor relaxation at depolarized voltages whether or not the pore gate has opened and that, after gate opening, voltage sensor relaxation contributes to the dramatic slowing of deactivation that we observe. Despite enhanced voltage sensor relaxation, CSI would be significantly impaired, because the pore gate, which blocks ion flow in the inactivated conformation, remains open. Gating current or voltage clamp fluorimetry experiments will be needed to investigate whether voltage sensor relaxation occurs from the open state in V404M channels.

Because V404M is located in S6, its influence on voltage sensor relaxation would be mediated by an allosteric mechanism (55). A likely possibility is that increased physical coupling between the pore gate and the voltage sensor domain in V404M channels promotes relaxation. This idea accords well with our evidence that the size-compensating E323D mutation, which presumably reverses increased physical coupling between the pore gate and the voltage sensor domain, rescues the functional effects of the V404M mutation that are evident both before and after pore opening.

**V404M Is Expected to Significantly Alter Neuronal Excitability and Synaptic Plasticity.** In neurons, Kv4.2 assembles with KChIP and DPP subunits to form $I_{SA}$ channels (8, 36–38). In twin boys carrying the V404M mutation, $I_{SA}$ channels will contain a mixture of mutant and wild-type Kv4.2 subunits. The functional effects of V404M are dominant in channels containing both V404M and wild-type subunits and are evident in the presence of KChIP and DPP subunits (1). In neurons, therefore, the V404M mutation would be expected to have complex, voltage-dependent effects on excitability and synaptic plasticity. Enhanced inactivation of closed channels might lead to greater resting inactivation and higher basal excitability. After subthreshold excitatory synaptic activity, slower recovery from inactivation might increase the window for coincidence detection in mechanisms of spike timing-dependent plasticity, resulting in inappropriate changes in synaptic strength. In response to suprathreshold stimuli, firing activity after the first spike might be dramatically suppressed by slow channel closure. Although it is difficult to predict in detail the effects of the V404M mutation on emergent neuronal properties, altered CSI gating is predicted to dramatically impact excitability and synaptic plasticity. This strongly supports the proposal that the Kv4.2 mutation underlies the etiology of epilepsy, autism, and intellectual disability in the affected twins (1).

In human neurons, which live at 37 °C, changes in the expression, trafficking, and posttranslational modification of V404M-containing $I_{SA}$ channels may also contribute to the clinical phenotype. Such effects are not evident in oocytes at 18 °C.

**Dominant Gain-of-Function Gating Mutations Are Associated with Early-Onset Neurological Diseases.** In contrast to the severe clinical consequences of the V404M mutation, which has dominant gain-of-function effects on CSI gating (1), the consequences of deleting the *Kcnd2* gene in mice are surprisingly mild (7, 56). The lack of dramatic phenotype was unexpected given the role of Kv4.2 in generating $I_{SA}$ currents in the brain and transient outward currents ($I_{to}$) in the heart (5, 7, 8, 56, 57). This suggests that gene deletion can be reasonably well-compensated by altering the expression of other channels. In contrast, the severe clinical phenotype associated with V404M in humans suggests that it is significantly more difficult to compensate for the effects of dominant gain-of-function mutations that alter essential gating properties, such as CSI. Kv3.3 provides a second example of this phenomenon. Kv3.3, like other Kv3 channels, has specialized gating properties that promote sustained, high-frequency firing in neurons (58). In cerebellar Purkinje neurons, Kv3.3 contributes to spontaneous pace-making activity (59, 60). Interestingly, dominant gain-of-function mutations that alter the specialized gating properties of Kv3.3 channels cause infant-onset spinocerebellar ataxia type 13 characterized by substantial cerebellar atrophy in the first few years of life, motor delay, persistent locomotor deficits, and intellectual disability (61–63). In contrast, Kv3.3 knockout mice have subtle phenotypes (64, 65). Although mice with genetic deletions of Kv genes have been extensively analyzed, relatively little is known about the effects of dominant gain-of-function gating mutations on neuronal excitability, synaptic plasticity, and circuit function in vivo. Because such mutations may be associated with infant-onset neurological diseases, this is an important area for future investigation.

## Materials and Methods

**Channel Expression and Electrophysiology.** All animal procedures were approved by the Chancellor's Animal Research Committee at the University of California, Los Angeles. Use of cloned human DNA sequences has been approved by the Institutional Biosafety Committee at the University of California, Los Angeles.

Plasmid cDNA clones of human *KChIP3a* and *DPP6s* were provided by Paul J. Pfaffinger, Baylor College of Medicine, Houston, and Manuel Covarrubias, Thomas Jefferson University, Philadelphia, respectively (36, 66). RNA encoding wild-type or mutant Kv4.2 was mixed at a 1:1 molar ratio with RNA encoding KChIP3a and injected into *Xenopus laevis* oocytes for functional analysis using a two-electrode voltage clamp (43, 44).

Data are provided as mean ± SEM. Statistical significance was analyzed by one-way ANOVA followed by Student's *t* test. For comparisons of three or more groups, using Student's *t* test or the Bonferroni post hoc correction did not alter which results were statistically significant.

Additional details are provided in *SI Materials and Methods*.

**Kinetic Modeling and Simulations.** Kinetic modeling and simulation of experimental data were performed using IChMASCOT (www.jadesantiago.com/Electrophysiology/IChMASCOT/) and IonChannelLab (67) based on a previously published gating model for Kv4.3 expressed with KChIP1 (40). This model was modified by eliminating inactivated states $I_5$ and $I_6$ arising from the open state. Data from wild-type channels were fitted using IChMASCOT, setting the initial values of kinetic parameters to those of Beck et al. (40). After fixing the $\alpha_{(V)}$ and $\beta_{(V)}$ rate constants to the fitted wild-type values, V404M data were fitted. Fitting was simultaneously constrained by five representative datasets each for the wild type and V404M, corresponding to a current–voltage (IV) series, prepulse inactivation traces, deactivation tail currents, inactivation onset at −60 mV, and recovery from inactivation at −120 mV (Fig. 8). Simulations of experimental data were performed using IonChannelLab (67). Peak occupancy of open and inactivated states was estimated from IonChannelLab simulations (67).

**ACKNOWLEDGMENTS.** We thank Drs. Paul Pfaffinger and Manuel Covarrubias for clones. We thank Dr. Jui-Yi Hsieh for comments on the manuscript. This work was supported by NIH Grant R01GM43459 (to D.M.P.) and the Department of Physiology at the University of California, Los Angeles.

1. Lee H, Lin MC, Kornblum HI, Papazian DM, Nelson SF (2014) Exome sequencing identifies de novo gain of function missense mutation in KCND2 in identical twins with autism and seizures that slows potassium channel inactivation. *Hum Mol Genet* 23:3481–3489.
2. Serôdio P, Vega-Saenz de Miera E, Rudy B (1996) Cloning of a novel component of A-type $K^+$ channels operating at subthreshold potentials with unique expression in heart and brain. *J Neurophysiol* 75:2174–2179.
3. Serôdio P, Rudy B (1998) Differential expression of Kv4 $K^+$ channel subunits mediating subthreshold transient $K^+$ (A-type) currents in rat brain. *J Neurophysiol* 79:1081–1091.
4. Rhodes KJ, et al. (2004) KChIPs and Kv4 $\alpha$ subunits as integral components of A-type potassium channels in mammalian brain. *J Neurosci* 24:7903–7915.
5. Jerng HH, Pfaffinger PJ, Covarrubias M (2004) Molecular physiology and modulation of somatodendritic A-type potassium channels. *Mol Cell Neurosci* 27:343–369.
6. Menegola M, Trimmer JS (2006) Unanticipated region- and cell-specific down-regulation of individual KChIP auxiliary subunit isotypes in Kv4.2 knock-out mouse brain. *J Neurosci* 26:12137–12142.
7. Chen X, et al. (2006) Deletion of Kv4.2 gene eliminates dendritic A-type $K^+$ current and enhances induction of long-term potentiation in hippocampal CA1 pyramidal neurons. *J Neurosci* 26:12143–12151.
8. Jerng HH, Pfaffinger PJ (2014) Modulatory mechanisms and multiple functions of somatodendritic A-type $K^+$ channel auxiliary subunits. *Front Cell Neurosci* 8:82.
9. Johnston D, et al. (2000) Dendritic potassium channels in hippocampal pyramidal neurons. *J Physiol* 525:75–81.
10. Bähring R, Covarrubias M (2011) Mechanisms of closed-state inactivation in voltage-gated ion channels. *J Physiol* 589:461–479.
11. Hoffman DA, Magee JC, Colbert CM, Johnston D (1997) $K^+$ channel regulation of signal propagation in dendrites of hippocampal pyramidal neurons. *Nature* 387: 869–875.
12. Migliore M, Hoffman DA, Magee JC, Johnston D (1999) Role of an A-type $K^+$ conductance in the back-propagation of action potentials in the dendrites of hippocampal pyramidal neurons. *J Comput Neurosci* 7:5–15.
13. Watanabe S, Hoffman DA, Migliore M, Johnston D (2002) Dendritic $K^+$ channels contribute to spike-timing dependent long-term potentiation in hippocampal pyramidal neurons. *Proc Natl Acad Sci USA* 99:8366–8371.
14. Ramakers GMJ, Storm JF (2002) A postsynaptic transient $K^+$ current modulated by arachidonic acid regulates synaptic integration and threshold for LTP induction in hippocampal pyramidal cells. *Proc Natl Acad Sci USA* 99:10144–10149.
15. Cai X, et al. (2004) Unique roles of SK and Kv4.2 potassium channels in dendritic integration. *Neuron* 44:351–364, and erratum (2004) 44:741.
16. Kim J, Wei DS, Hoffman DA (2005) Kv4 potassium channel subunits control action potential repolarization and frequency-dependent broadening in rat hippocampal CA1 pyramidal neurones. *J Physiol* 569:41–57.
17. Truchet B, et al. (2012) Kv4 potassium channels modulate hippocampal EPSP-spike potentiation and spatial memory in rats. *Learn Mem* 19:282–293.
18. Long SB, Campbell EB, MacKinnon R (2005) Crystal structure of a mammalian voltage-dependent Shaker family $K^+$ channel. *Science* 309:897–903.
19. Seoh SA, Sigg D, Papazian DM, Bezanilla F (1996) Voltage-sensing residues in the S2 and S4 segments of the Shaker $K^+$ channel. *Neuron* 16:1159–1167.
20. Aggarwal SK, MacKinnon R (1996) Contribution of the S4 segment to gating charge in the Shaker $K^+$ channel. *Neuron* 16:1169–1177.
21. Dougherty K, De Santiago-Castillo JA, Covarrubias M (2008) Gating charge immobilization in Kv4.2 channels: The basis of closed-state inactivation. *J Gen Physiol* 131: 257–273.
22. Barghaan J, Bähring R (2009) Dynamic coupling of voltage sensor and gate involved in closed-state inactivation of Kv4.2 channels. *J Gen Physiol* 133:205–224.
23. Bähring R, Barghaan J, Westermeier R, Wollberg J (2012) Voltage sensor inactivation in potassium channels. *Front Pharmacol* 3:100.
24. Fineberg JD, Ritter DM, Covarrubias M (2012) Modeling-independent elucidation of inactivation pathways in recombinant and native A-type Kv channels. *J Gen Physiol* 140:513–527.
25. Fineberg JD, Szanto TG, Panyi G, Covarrubias M (2016) Closed-state inactivation involving an internal gate in Kv4.1 channels modulates pore blockade by intracellular quaternary ammonium ions. *Sci Rep* 6:31131.
26. Jerng HH, Shahidullah M, Covarrubias M (1999) Inactivation gating of Kv4 potassium channels: Molecular interactions involving the inner vestibule of the pore. *J Gen Physiol* 113:641–660.
27. Zagotta WN, Hoshi T, Aldrich RW (1994) Shaker potassium channel gating. III: Evaluation of kinetic models for activation. *J Gen Physiol* 103:321–362.
28. Holmgren M, Shin KS, Yellen G (1998) The activation gate of a voltage-gated $K^+$ channel can be trapped in the open state by an intersubunit metal bridge. *Neuron* 21: 617–621.
29. Webster SM, Del Camino D, Dekker JP, Yellen G (2004) Intracellular gate opening in Shaker $K^+$ channels defined by high-affinity metal bridges. *Nature* 428:864–868.
30. Yifrach O, MacKinnon R (2002) Energetics of pore opening in a voltage-gated $K^+$ channel. *Cell* 111:231–239.
31. Lu Z, Klem AM, Ramu Y (2002) Coupling between voltage sensors and activation gate in voltage-gated $K^+$ channels. *J Gen Physiol* 120:663–676.
32. Wollberg J, Bähring R (2016) Intra- and intersubunit dynamic binding in Kv4.2 channel closed-state inactivation. *Biophys J* 110:157–175.
33. Hoshi T, Zagotta WN, Aldrich RW (1990) Biophysical and molecular mechanisms of Shaker potassium channel inactivation. *Science* 250:533–538.
34. Zagotta WN, Hoshi T, Aldrich RW (1990) Restoration of inactivation in mutants of Shaker potassium channels by a peptide derived from ShB. *Science* 250:568–571.
35. Kiss L, Korn SJ (1998) Modulation of C-type inactivation by $K^+$ at the potassium channel selectivity filter. *Biophys J* 74:1840–1849.
36. Jerng HH, Kunjilwar K, Pfaffinger PJ (2005) Multiprotein assembly of Kv4.2, KChIP3 and DPP10 produces ternary channel complexes with $I_{SA}$-like properties. *J Physiol* 568:767–788.
37. Amarillo Y, et al. (2008) Ternary Kv4.2 channels recapitulate voltage-dependent inactivation kinetics of A-type $K^+$ channels in cerebellar granule neurons. *J Physiol* 586: 2093–2106.
38. Covarrubias M, et al. (2008) The neuronal Kv4 channel complex. *Neurochem Res* 33: 1558–1567.
39. An WF, et al. (2000) Modulation of A-type potassium channels by a family of calcium sensors. *Nature* 403:553–556.
40. Beck EJ, Bowlby M, An WF, Rhodes KJ, Covarrubias M (2002) Remodelling inactivation gating of Kv4 channels by KChIP1, a small-molecular-weight calcium-binding protein. *J Physiol* 538:691–706.
41. Pioletti M, Findeisen F, Hura GL, Minor DL, Jr (2006) Three-dimensional structure of the KChIP1-Kv4.3 T1 complex reveals a cross-shaped octamer. *Nat Struct Mol Biol* 13: 987–995.
42. Wang H, et al. (2007) Structural basis for modulation of Kv4 $K^+$ channels by auxiliary KChIP subunits. *Nat Neurosci* 10:32–39.
43. Timpe LC, et al. (1988) Expression of functional potassium channels from *Shaker* cDNA in *Xenopus* oocytes. *Nature* 331:143–145.
44. Papazian DM, Timpe LC, Jan YN, Jan LY (1991) Alteration of voltage-dependence of Shaker potassium channel by mutations in the S4 sequence. *Nature* 349:305–310.
45. Oxford GS (1981) Some kinetic and steady-state properties of sodium channels after removal of inactivation. *J Gen Physiol* 77:1–22.
46. Harpaz Y, Gerstein M, Chothia C (1994) Volume changes on protein folding. *Structure* 2:641–649.
47. Long SB, Tao X, Campbell EB, MacKinnon R (2007) Atomic structure of a voltage-dependent $K^+$ channel in a lipid membrane-like environment. *Nature* 450:376–382.
48. Heler R, Bell JK, Boland LM (2013) Homology model and targeted mutagenesis identify critical residues for arachidonic acid inhibition of Kv4 channels. *Channels (Austin)* 7:74–84.
49. Villalba-Galea CA, Sandtner W, Starace DM, Bezanilla F (2008) S4-based voltage sensors have three major conformations. *Proc Natl Acad Sci USA* 105:17600–17607.
50. Labro AJ, Lacroix JJ, Villalba-Galea CA, Snyders DJ, Bezanilla F (2012) Molecular mechanism for depolarization-induced modulation of Kv channel closure. *J Gen Physiol* 140:481–493.
51. Olcese R, Sigg D, Latorre R, Bezanilla F, Stefani E (2001) A conducting state with properties of a slow inactivated state in a Shaker $K^+$ channel mutant. *J Gen Physiol* 117:149–163.
52. Piper DR, Varghese A, Sanguinetti MC, Tristani-Firouzi M (2003) Gating currents associated with intramembrane charge displacement in HERG potassium channels. *Proc Natl Acad Sci USA* 100:10534–10539.
53. Labro AJ, Priest MF, Lacroix JJ, Snyders DJ, Bezanilla F (2015) Kv3.1 uses a timely resurgent $K^+$ current to secure action potential repolarization. *Nat Commun* 6:10173.
54. Pau V, Zhou Y, Ramu Y, Xu Y, Lu Z (2017) Crystal structure of an inactivated mutant mammalian voltage-gated $K^+$ channel. *Nat Struct Mol Biol* 24:857–865.
55. Haddad GA, Blunck R (2011) Mode shift of the voltage sensors in Shaker $K^+$ channels is caused by energetic coupling to the pore domain. *J Gen Physiol* 137:455–472.
56. Guo W, et al. (2005) Targeted deletion of Kv4.2 eliminates $I_{(to,f)}$ and results in electrical and molecular remodeling, with no evidence of ventricular hypertrophy or myocardial dysfunction. *Circ Res* 97:1342–1350.
57. Nerbonne JM, Kass RS (2005) Molecular physiology of cardiac repolarization. *Physiol Rev* 85:1205–1253.
58. Rudy B, McBain CJ (2001) Kv3 channels: Voltage-gated $K^+$ channels designed for high-frequency repetitive firing. *Trends Neurosci* 24:517–526.
59. Martina M, Yao GL, Bean BP (2003) Properties and functional role of voltage-dependent potassium channels in dendrites of rat cerebellar Purkinje neurons. *J Neurosci* 23:5698–5707.
60. Akemann W, Knöpfel T (2006) Interaction of Kv3 potassium channels and resurgent sodium current influences the rate of spontaneous firing of Purkinje neurons. *J Neurosci* 26:4602–4612.
61. Waters MF, et al. (2006) Mutations in the voltage-gated potassium channel KCNC3 cause degenerative and developmental CNS phenotypes. *Nat Genet* 38: 447–451.
62. Minassian NA, Lin MC, Papazian DM (2012) Altered Kv3.3 channel gating in early-onset spinocerebellar ataxia type 13. *J Physiol* 590:1599–1614.
63. Duarri A, et al. (2015) Functional analysis helps to define KCNC3 mutational spectrum in Dutch ataxia cases. *PLoS One* 10:e0116599.
64. Espinosa F, et al. (2001) Alcohol hypersensitivity, increased locomotion, and spontaneous myoclonus in mice lacking the potassium channels Kv3.1 and Kv3.3. *J Neurosci* 21:6657–6665.
65. Matsukawa H, Wolf AM, Matsushita S, Joho RH, Knöpfel T (2003) Motor dysfunction and altered synaptic transmission at the parallel fiber-Purkinje cell synapse in mice lacking potassium channels Kv3.1 and Kv3.3. *J Neurosci* 23:7677–7684.
66. Jerng HH, Qian Y, Pfaffinger PJ (2004) Modulation of Kv4.2 channel expression and gating by dipeptidyl peptidase 10 (DPP10). *Biophys J* 87:2380–2396.
67. Santiago-Castillo JA, Covarrubias M, Sánchez-Rodríguez JE, Perez-Cornejo P, Arreola J (2010) Simulating complex ion channel kinetics with IonChannelLab. *Channels (Austin)* 4:422–428.